Direct Observation of a Localized Flat-Band State in a Mapped Moiré Hubbard Photonic Lattice

Hui-Min Lin,[1,2,†] Yong-Heng Lu,[1,2,†] Yi-Jun Chang,[1,2] Ying-Yue Yang,[1,2] and Xian-Min Jin[1,2,3,4,*]

[1] *Center for Integrated Quantum Information Technologies (IQIT), School of Physics and Astronomy and State Key Laboratory of Advanced Optical Communication Systems and Networks, Shanghai Jiao Tong University, Shanghai 200240, China*

[2] *CAS Center for Excellence and Synergetic Innovation Center in Quantum Information and Quantum Physics, University of Science and Technology of China, Hefei, Anhui 230026, China*

[3] *TuringQ Co. Ltd., Shanghai 200240, China*

[4] *Chip Hub for Integrated Photonics Xplore (CHIPX), Shanghai Jiao Tong University, Wuxi 214000, China*

(Received 5 January 2022; revised 13 August 2022; accepted 30 August 2022; published 3 November 2022)

When two identical periodic structures are stacked at a series of discrete rotation angles, the resulting moiré pattern brings an extreme flat band with transport enhancement. It provides insights into the fascinating physics of insulating states and unconventional superconductivity with delocalization-localization transitions and commensurable-incommensurable phases. However, the exploration of symmetry- and geometry-independent flat-band physics with moiré patterns is still rare, limited by the stringent requirement in high dimension. Here, we experimentally observe the localized flat-band state by mapping a moiré model into a one-dimensional photonic lattice using a femtosecond laser direct writing technique. By accurately controlling the external periodic field, we construct moiré photonic lattices with different moiré band structures. We successfully observe the photon-walker evolution from splitting with dispersion to nondispersive propagation with larger localization in the input ports as the result of a flat band induced by moiré patterns with larger period. Our approach to engineering moiré model, together with the integrated photonic implementation, establishes a powerful tool for exploring the effects accompanying the transition from commensurate to incommensurate phases.

DOI: 10.1103/PhysRevApplied.18.054012

I. INTRODUCTION

A moiré pattern consists of two superimposed copies of a periodic structure with a slightly twisted angle [1]. The periodicity of such a moiré pattern leads to moiré Bloch bands [2]. For a discrete set of magic angles, the lowest moiré band flattens, which induces commensurable-incommensurable transitions and topological defects [3], insulating states [4], superconductivity [5,6], the quantum Hall effect [7], and the realization of non-Abelian gauge potentials [8]. Moiré patterns have been usually produced in a high dimension, using graphene aligned to hexagonal boron nitride [9,10], twisted multilayer graphene [11,12], and graphene on silicon carbide [13]. The customary approach to access the flat band with moiré pattern mainly focuses on fabricating accurate magic angles [14–16] or applying high external pressure in a graphene-based system [17–19]. However, it is still challenging to realize the flat band with moiré pattern because of the stringent requirement with once-determined formation in high dimension.

Two periodic ingredients of a moiré pattern can come from inherent crystalline order and periodic external field [20]. A one-dimensional moiré system with different moiré patterns [21], corresponding to commensurable and incommensurable phases, is considered as a potential candidate to access the flat band for exploring the rich moiré physics [22–24]. Moiré patterns, corresponding to the incommensurate phase, may enable the localization of light because of the existence of extremely flat bands [25,26], which strongly links to the structural periodicity properties instead of the traditional highly symmetrical geometry [27,28].

Recently, photonic integrated waveguide systems have provided a versatile platform to explore various artificial structures and different topological models [29–32]. The manipulation and manifestation of the wave function and band modes can be appropriately mapped to certain observables in real space with appropriate excitation conditions [33,34]. Highly designable capabilities and physical scalability of the photonic lattice [35–37] enable it to meet the challenging requirements of the moiré

*xianmin.jin@sjtu.edu.cn

†These authors contributed equally to this work.

photonic lattice with the hidden physics of flat bands. The mapping between band states and photonic lattices can be extended to highly complex artificial structures, which, fascinatingly, can make it possible to directly observe the flat band states in a moiré model.

In this work, we successfully observe compact localized state based on flat band in a one-dimensional moiré photonic lattice using a femtosecond laser direct writing technique [38,39]. With the modulation of the external periodic field, we are able to construct photonic lattices of the moiré system, which induces commensurable and incommensurable moiré patterns. For a large-period moiré system, we observe the photon-walker evolution from dispersive propagation to dispersionless, and from splitting to higher confinement in input ports.

II. MODEL

The moiré system is based on a one-dimensional model with nearest-neighbor coupling, as shown in Fig. 1(a). The Hamiltonian of the moiré system can be described by

$$H_0 = \sum_{m=1}^{M}\Bigg[\sum_{n=1}^{N-1} J\left(c_{m,n}^{+}c_{m,n+1} + \text{H.c.}\right) + c_{m,N}^{\dagger}c_{m+1,1} + \text{H.c.} + \sum_{n=1}^{N} A_n c_{m,n}^{+}c_{m,n}\Bigg], \quad (1)$$

where $c_{m,n}^{+}$ ($c_{m,n}$) is the bosonic creation (annihilation) operator at site n in the mth unit cell and J represents the nearest-neighbor coupling strength. Spatially modulated on-site potential $A_n = (-1)^n V\cos(\pi n/n_0)$ is commensurate with the moiré period $N = 2n_0$, which is different from the Aubry-André model based on quasiperiodic on-site potential, as shown in Fig. 1(b). The model is a uniform chain modulated by a cosinusoidal-period external field, making high-dimensional system map to one dimension.

The evolution of photons in the photonic lattice is governed by the Schrödinger equation, which is mathematically equivalent to the paraxial wave equation (see Appendix A for the derivation of evolution equation for photonic lattice):

$$i\partial_z\psi_i(z) = \sum_j H_{ij}^{\text{TB}}\psi_j(z), \quad (2)$$

where z corresponds to the evolution distance in the propagation direction of the photonic lattice. The one-dimensional moiré model, only considering the nearest coupling, well matches the tight-binding model. Therefore, the exquisitely designable photonic lattice of the moiré system makes it possible to explore the rich moiré physics.

III. FLAT-BAND STATE

Considering a periodic boundary condition $c_{M+1,1} = c_{1,1}$, the Hamiltonian can be diagonalized by Fourier transformation $c_{m,n} = 1/\sqrt{M}\sum_k e^{ikm}c_{k,n}$:

$$H_0 = \sum_k\Bigg[\sum_{n=1}^{N-1} J\left(c_{k,n}^{+}c_{k,n+1} + \text{H.c.}\right) + c_{k,N}^{+}c_{k+1,1}e^{ik} + \text{H.c.} + \sum_{n=1}^{N} A_n c_{k,n}^{+}c_{k,n}\Bigg], \quad (3)$$

where $k = 2l\pi/M, l = 0, 1, \ldots, M-1$. The above Hamiltonian has $N = 2n_0$ bands, and each band gives a spectrum versus k. We select two bands around zero energy of the one-dimensional moiré system with moiré period $N =$ 60, 100, 200, and 400, shown in Figs. 2(a1)–2(d1). As the moiré period N increases, the slope of the band gradually becomes lower and tends to zero. Here, for the larger moiré period, two different energy bands degenerately merge to one zero-energy mode in the middle of the band structure. The nearly extreme flat band can be obtained in the case of moiré period $N = 400$. The appearance of the flat band is related to commensurate periodicity with moiré physics applied by the external field in lower-dimensional system rather than the requirement of high symmetry with highly symmetric points [27,28,35].

We further extract the two midgap wave functions in a single moiré unit cell with $k = 0$, as shown in Figs. 2(a2)–2(d2) and 2(a3)–2(d3). The width of the wave packet relatively decreases as the moiré period increases and the overlap between two adjacent wave packets totally disappears at moiré period $N = 400$. At the same time, the state becomes a separate Gaussian wave packet with the center located at the point $n_0/2$ and $3n_0/2$ with zero potential energy.

The flat band with narrow bandwidth is a completely nondispersive band in the spectrum [40], which is accompanied by the significant feature of a compact localized state [41,42]. With injecting the desired input state into the middle site with zero on-site potential of the photonic lattice, we simulate the result of outgoing photon distribution in one-dimensional moiré photonic lattices, as shown in Figs. 3(a)–3(e). When setting the moiré period at 60, the photon state experiences obvious wave-packet splitting and diffraction-range broadening with two separated parts and two local peaks far from the input ports, which is governed by the dispersion band in small moiré periodic patterns [see Fig. 3(a)]. As the moiré period increases, the two separated photon states move toward each other and show the process of moving and merging, resulting in a Gaussian wave packet with the center located at the input ports. Due to the large moiré period (from $N = 400$ to $N =$ 1000) with the existence of extreme flat band, the propagation of photons remains more confined than for the case of

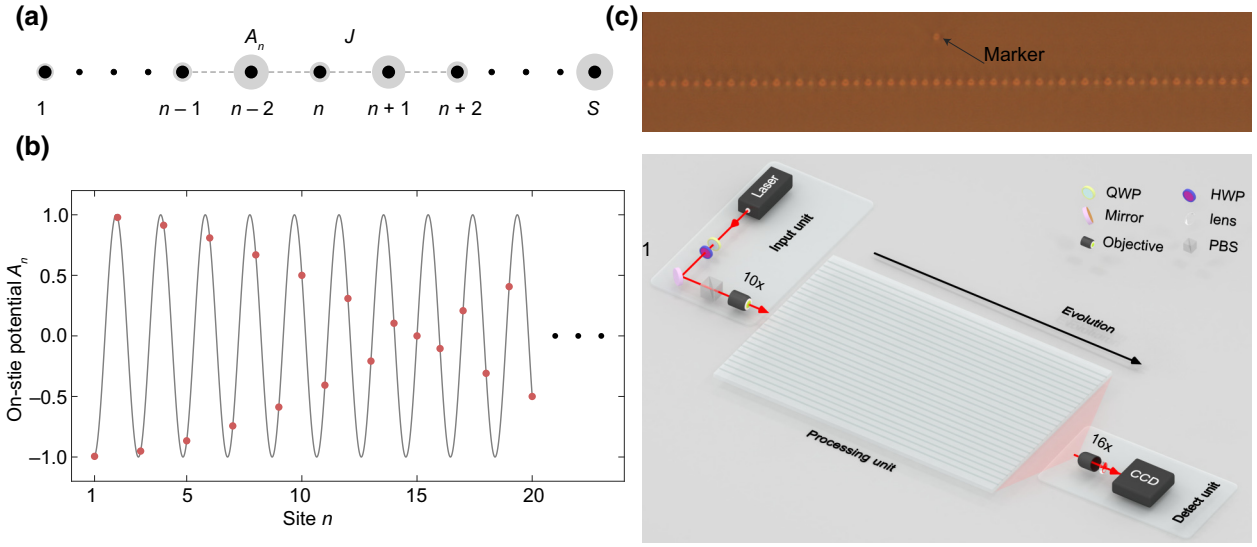

FIG. 1. Constructing a one-dimensional moiré system on a photonic chip. (a) Schematic illustration of the photonic lattice. A one-dimensional moiré system consists of two ingredients with slightly different periods for on-site potential. The adjacent coupling strength is $J = 1\ \mathrm{mm}^{-1}$. (b) The on-site potential distribution is spatially modulated as $A_n = (-1)^n V \cos(\pi n/n_0)$, which can be realized by a cosinusoidal function $\cos[(1 + 1/n_0)\pi x]$ when $n = \mathrm{INT}(x)$. Here the moiré period $N = 60$ and $V = 1$. (c) Cross section microgram of the photonic lattice and experimental setup. The marker is designed to record the excited site. The photons are injected into the photonic chip using a 10× input lens (NA = 0.16) and the output distribution is captured by a 16× input lens (NA = 0.25) and a charge coupled device (CCD). QWP, quarter-wave plate; HWP, half-wave plate; PBS, polarization beam splitter.

small moiré period at the input ports, which visualizes the midgap flat band with localized wave functions.

IV. MAPPED MOIRÉ PHOTONIC LATTICES

To experimentally observe the flat-band states, we fabricate moiré photonic lattices by mapping the Hamiltonian with moiré patterns into a $20 \times 50 \times 1$ mm borosilicate glass by a femtosecond laser direct writing technique [see Fig. 1(c)]. Each photonic lattice contains 201 waveguides, with modulation of periodic cosinusoidal on-site potential of different moiré period N. On-site potential of the moiré model is realized by modulating the refractive index of the waveguide, which can be tuned by scanning velocity or laser power [43]. We accurately control the on-site potential by tuning the laser power to achieve the accessible wide range from -1 to $1\ \mathrm{mm}^{-1}$ of A_n. The spacing between adjacent waveguides is designed as 7.73 μm corresponding to coupling strength of $J = 1\ \mathrm{mm}^{-1}$ (see Appendix B for the modulation details of coupling strength and on-site potential). The middle site is set as the zero-energy potential point. A Gaussian wave packet with a width of five waveguides is injected into the middle site of the photonic lattice. After propagating through 50 mm, the outgoing light distribution is captured by a CCD camera.

We experimentally image the photon evolution patterns for four moiré periods ($N = 60, 100, 200$, and 400), as shown in Figs. 4(a)–4(d). The photons propagate dispersively with two separated local parts far from the input sites in the case of moiré period $N = 60$. There are almost no photons confined in the input region. It is obvious that the photons become concentrated in the input region in the case of larger moiré period N. For a moiré period of 400, we observe the higher confinement of photons staying inside the input regions, which reveals the moving and merging of the two separated photon wave packets governed by the nondispersive flat-band states.

The corresponding outgoing intensity distribution is normalized, shown in Figs. 4(f)–4(i). To further quantify the confinement of photons in the given input region for the zero-energy state, we introduce the generalized return probability defined as: $\xi = \sum_{i=j-d}^{j+d} I_i / \sum_{i=1}^{n} I_i$ [44]. It characterizes the probability of photons staying inside a small injected region from the injected point j. Here $d = 2$ corresponds to the width of the injected Gaussian wave packet. I is the intensity of the photons in site i and n is the total number of sites in the lattice.

For a range of relatively small moiré periods, the generalized return probability rapidly increases as the moiré period becomes larger. When the moiré period reaches $N = 400$, the generalized return probability becomes stably high, indicating the existence of the extreme flat-band state. The experimental quantity is $\xi_{N=60} = 0.0384$, $\xi_{N=100} = 0.0995$, $\xi_{N=200} = 0.1276$, and $\xi_{N=400} = 0.1338$. The consistency with the expected simulation shows the gathering of photons in the input sites as the moiré period becomes larger. The experimental results are further statistically analyzed and verified by considering the fabrication

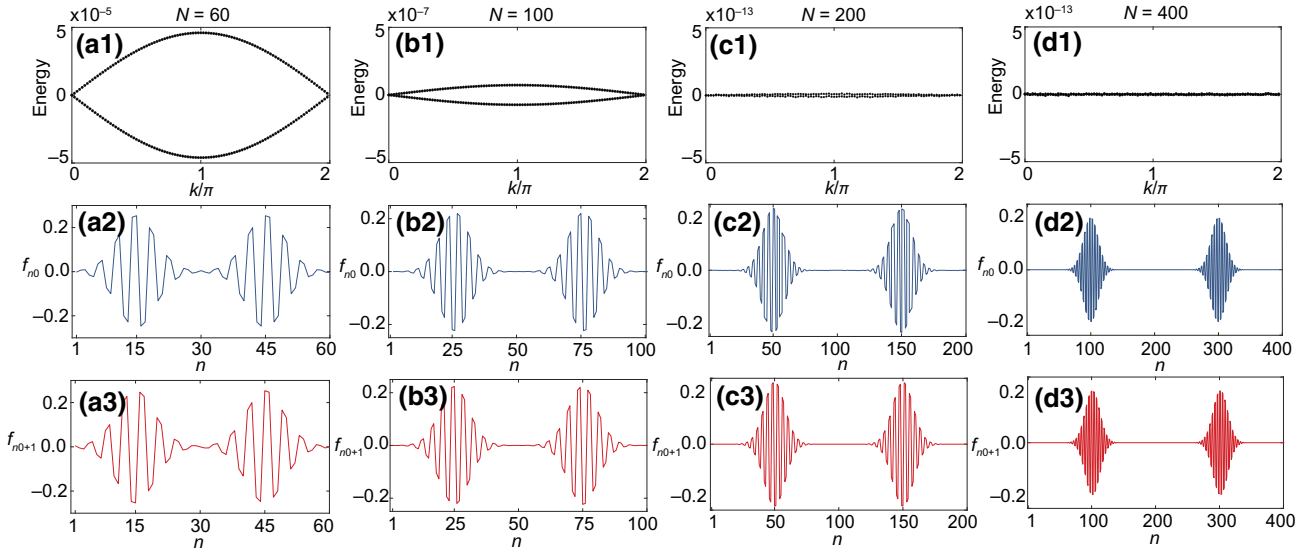

FIG. 2. Spectrum of moiré lattice with localized flat-band state. (a1)–(d1) Selected spectra around zero energy and (a2)–(d2) and (a3)–(d3) midgap wave functions for the moiré system with moiré period $N = 60, 100, 200$, and 400. We present the midgap wave functions in a single moiré unit cell with $k = 0$. As the moiré period N increases, the midgap band becomes a nearly nondispersive band [(a1)–(d1)]. At the same time, the width of the wave packet decreases, and the overlap between two adjacent wave packets disappears [(a2)–(d2) and (a3)–(d3)]. The parameters of the moiré system are $V = 1, J = 1\ \text{mm}^{-1}$, and $M = 100$.

fluctuation of photonic lattices [see Fig.4(e)]. The uncertainty originates from the fluctuation of focus position and laser power of the femtosecond laser, and resulting spacing fluctuates around $l = 7.73 \pm 0.15\ \mu$m (disorder $c \pm 0.05\ \text{mm}^{-1}$) and power fluctuates around $w \pm 0.05$ mW ($\beta \pm 0.05\ \text{mm}^{-1}$).

The comparison of the experimental photon patterns and numerical simulation can be characterized by similarity, defined as $F = \sum_i \sqrt{s_i t_i}$, where s and t are the theoretical and experimental intensity distributions, respectively. The calculated similarity is $F_{N=60} = 0.8328$, $F_{N=100} = 0.8382$, $F_{N=200} = 0.7975$, and $F_{N=400} = 0.7661$, which indicates that we observe the tendency of photon behaviors from dispersive evolution to nondispersive evolution with the existence of flat band when the moiré period increases. Therefore, we successfully demonstrate the observation of localized flat-band states for large moiré period in a mapped moiré photonic lattice.

V. CONCLUSION

In conclusion, we experimentally observe localized flat-band states for a large enough moiré period N. By constructing a one-dimensional photonic moiré lattice, we successfully demonstrate an artificial simulator access to the flat band by controlling the period of the moiré

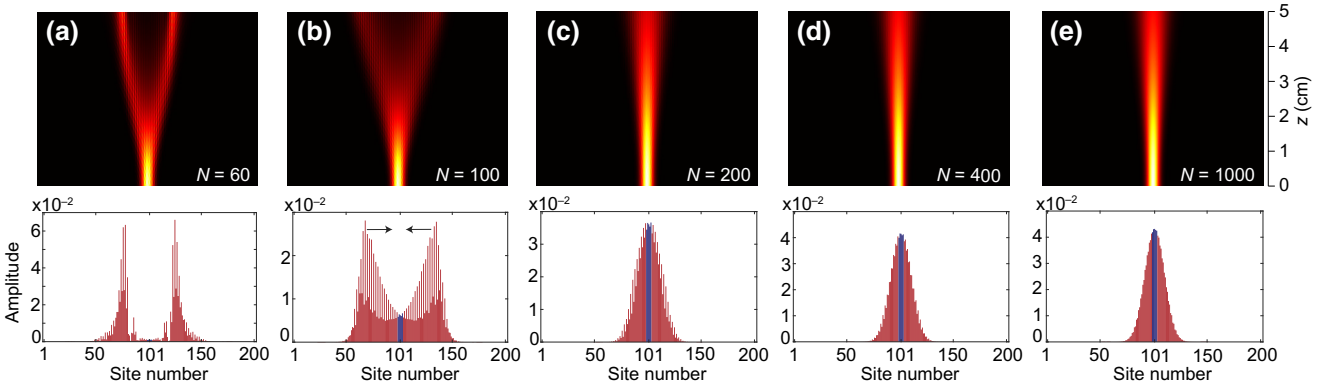

FIG. 3. Simulation results of localized flat-band state. The simulated outgoing intensity distribution of photons (top row) and the cross section of the simulation result (bottom row) for a photonic lattice according to the one-dimensional moiré model with moiré period (a) $N = 60$, (b) $N = 100$, (c) $N = 200$, (d) $N = 400$, and (e) $N = 1000$. The evolution distance is 50 mm. The blue region marks the input position.

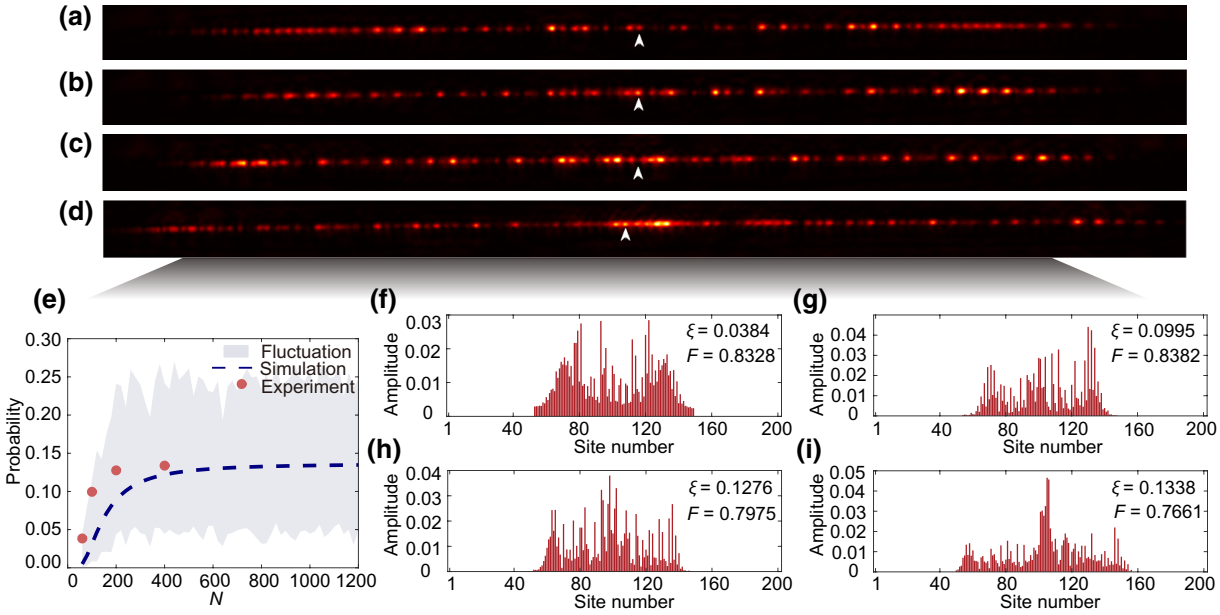

FIG. 4. Experimental results of observing localized flat-band state. (a)–(d) Experimentally output images for four typical moiré periods $N = 60, 100, 200$, and 400, respectively. (f)–(i) The outgoing intensity distribution of (a)–(d). The intensity distribution is normalized. The parameters are the same as those of the simulation. (e) The generalized return probability. Statistically, the shaded region shows one standard deviation away from the averaged localization level obtained from 100 random simulations with disorder $c \pm 0.05$ mm^{-1} and $\beta \pm 0.05$ mm^{-1}. The values of generalized return probability ξ and similarity F are shown in (f)–(i).

system. Our work experimentally presents an easily accessible approach to explore the transition between dispersive and nondispersive physics through accurately controlling the periodic external field.

In the future, combined with the successful mapped moiré system with flat bands in this work and the possible introduction of extended Bose-Hubbard Hamiltonian [45,46] for the photonic lattices, it may pave the way to explore superconductivity, correlated insulators, and other exotic quantum phases [47,48] in the photonic integrated system. Taking full advantage of superposition of compact localized states based on flat bands, it is of great interest to demonstrate image transmission without distortion in such a photonic lattice [49,50]. Furthermore, this approach has promising potential to explore other topological phenomena, such as topological phase-enabled protection [51].

ACKNOWLEDGMENTS

This research is supported by the National Key R&D Program of China (Grants No. 2019YFA0308700, No. 2019YFA0706302, and No. 2017YFA0303700); National Natural Science Foundation of China (NSFC) (Grants No. 11904229, No. 61734005, No. 11761141014, and No. 11690033); Science and Technology Commission of Shanghai Municipality (STCSM) (Grants No. 20JC1416300 and No. 2019SHZDZX01); Shanghai Municipal Education Commission (SMEC) (Grant No. 2017-01-07-00-02-E00049); and China Postdoctoral Science Foundation (Grant No. 2020M671091). X.-M.J. acknowledges additional support from Zhiyuan Innovative Research Center of Shanghai Jiao Tong University.

APPENDIX A: EVOLUTION IN PHOTONIC LATTICE

In this appendix, we give the detailed derivation of the equation in the main text describing the evolution

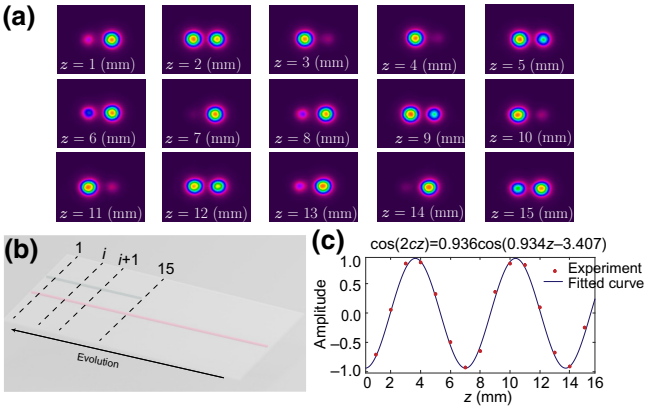

FIG. 5. Coupling strength. (a) The output photon patterns under different coupling lengths when the waveguide spacing is 10 μm. (b) Schematic diagram of the photonic chip for measuring the coupling strength. (c) Experimental measurement of the coupling strength c.

of photons in our system. The propagation of a light field through a medium can be described by the scalar Helmholtz equation [52]:

$$\nabla^2 E + k_0^2 n^2(x,z)E = 0. \tag{A1}$$

By inserting the solutions $E(x,z) = \psi(x,z)e^{i(\beta z+\omega\tau)}$, where $\beta = n_0 k_0$, we can obtain

$$i\frac{\partial\psi(x,z)}{\partial z} = -\frac{1}{2k_0 n_0}\nabla^2\psi(x,z) - \frac{k_0(n^2 - {n_0}^2)}{2n_0}\psi(x,z), \tag{A2}$$

where $n = n_0 + \Delta n$ is the refractive index of the waveguide. Δn is the refractive index change caused by processing. Ignoring the quadratic term of Δn, we obtain

$$i\frac{\partial\psi(x,z)}{\partial z} = -\frac{1}{2k_0 n_0}\nabla^2\psi(x,z) - k_0\Delta n(x,z)\psi(x,z). \tag{A3}$$

The obtained paraxial wave equation, Eq. (A3) (describing the evolution of photons in integrated waveguide arrays), is similar to the Schrödinger equation (describing the time evolution of electrons, which is equivalent to the evolution of photons along the propagation direction z in a photonic lattice) as [53]

$$i\hbar\partial_t\psi = -\frac{\hbar^2}{2\mu}\nabla^2\psi - U(x,y,z)\psi(x,y,z). \tag{A4}$$

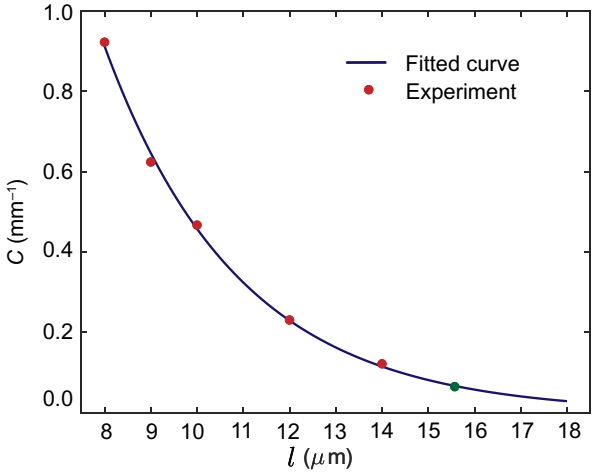

FIG. 6. The relationship of coupling strength c and waveguide spacing l. The green circle corresponds to coupling strength $c = 0.0697$ mm^{-1} at the next-nearest-neighbor distance $l = 15.46$ μm.

For Eq. (A3), ignoring the quadratic term of $\partial\psi(x,z)/\partial z$, we obtain

$$i\frac{\partial\psi(x,z)}{\partial z} = -\frac{1}{2k_0 n_0}\frac{\partial^2\psi(x,z)}{\partial x^2} - k_0\Delta n(x,z)\psi(x,z). \tag{A5}$$

To describe the evolution of photons in the waveguide system, we can employ the tight-binding approximation to the result for the waveguide system, and we obtain

$$\begin{aligned} i\frac{\partial\psi_n}{\partial z} &= -\frac{1}{2k_0 n_0}\left(\frac{\psi_{n-1} - 2\psi_n + \psi_{n+1}}{d^2}\right) - k_0\Delta n(x,z)\psi_n \\ &= -\frac{1}{2k_0 n_0 d^2}(\psi_{n-1} + \psi_{n+1}) - (k_0\Delta n(x,z) \\ &\quad - \frac{1}{k_0 n_0 d^2})\psi_n = -c(\psi_{n-1} + \psi_{n+1}) - \beta\psi_n \\ &= \dot{H}\psi_n, \end{aligned} \tag{A6}$$

where c is the coupling strength between the adjacent waveguides and β is the propagation constant, corresponding to the on-site potential. Thus, we finish the derivation of the evolution equation from the Helmholtz equation.

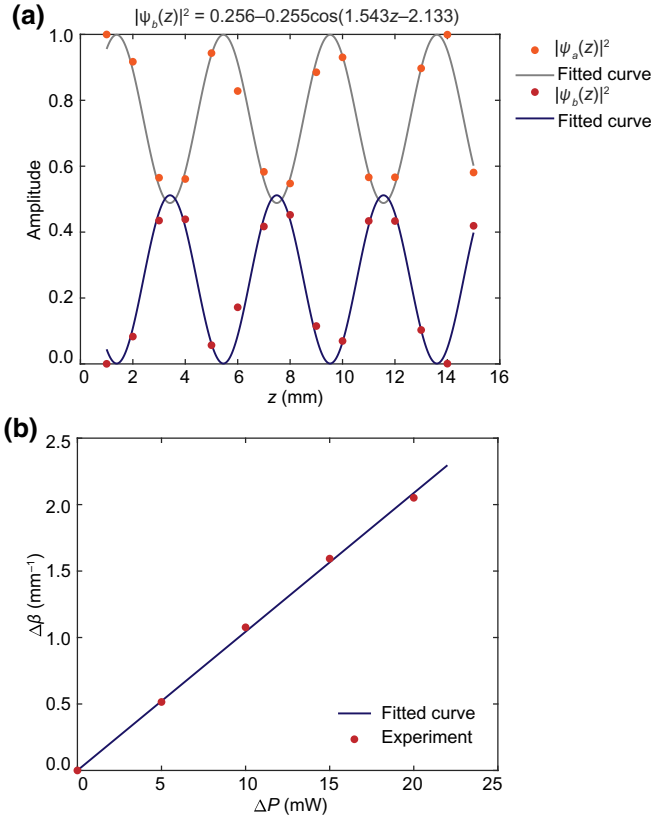

FIG. 7. Propagation constant. (a) Measurement of the propagation constant. (b) The relationship between propagation constant and laser power.

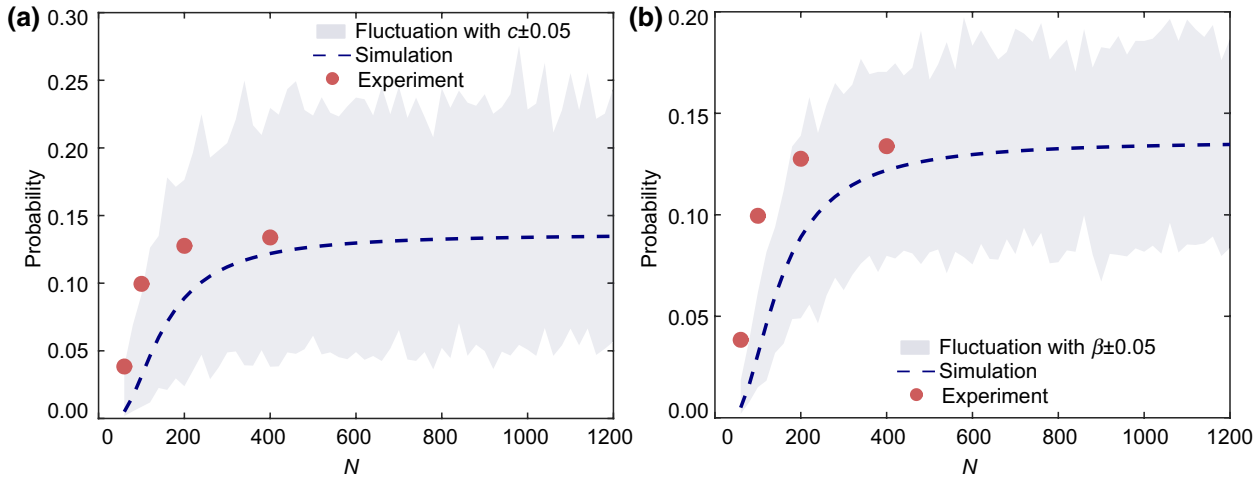

FIG. 8. The generalized return probability of simulation and experiment. Statistically, the shaded region shows one standard deviation away from the averaged localization level (the red circle) obtained from 100 simulations with disorder $c \pm 0.05$ mm^{-1} (a) and $\beta \pm 0.05$ mm^{-1} (b). The experimental parameters are the same as those in the simulation.

APPENDIX B: MODULATION OF COUPLING AND ON-SITE POTENTIAL

In this appendix, we demonstrate how to modulate the coupling strength and on-site potential. Consider the evolution of photons in a two-waveguide system [54]:

$$\begin{aligned} -i\tfrac{\partial\psi_a}{\partial z} &= \beta_a\psi_a + c\psi_b \\ -i\tfrac{\partial\psi_b}{\partial z} &= \beta_b\psi_b + c\psi_a. \end{aligned} \tag{B1}$$

For the same propagation constant ($\beta_a = \beta_b = \beta$):

$$\begin{aligned} \psi_a(z) &= [\cos(cz)\psi_a(0) + i\sin(cz)\psi_b(0)]e^{-i\beta z} \\ \psi_b(z) &= [\cos(cz)\psi_b(0) + i\sin(cz)\psi_a(0)]e^{-i\beta z}. \end{aligned} \tag{B2}$$

If the waveguide a is excited alone, the initial states $\psi_a(0) = 1$ and $\psi_b(0) = 0$. The probabilities of photons distributed in waveguide a and waveguide b are $|\psi_a(z)|^2 = |\cos(cz)|^2$ and $|\psi_b(z)|^2 = |\sin(cz)|^2$, respectively. According to the trigonometric relationship, we obtain

$$\frac{|\Psi_a(z)|^2 - |\Psi_b(z)|^2}{|\Psi_a(z)|^2 + |\Psi_b(z)|^2} = \frac{\cos^2(cz) - \sin^2(cz)}{\cos^2(cz) + \sin^2(cz)} = \cos(2cz). \tag{B3}$$

The relationship between the oscillation period of the photon intensity evolution in the two waveguides and the coupling strength c is $T = \pi/c$.

We measure the outgoing light spots of the two waveguides under different coupling lengths, as shown in Fig. 5(a). We substitute the processed outgoing spot intensities $|\psi_a(z)|^2$ and $|\psi_b(z)|^2$ into Eq. (B3), and then fit the curve to get the period. Then the coupling strength c is obtained [as shown in Fig. 5(c)]. Further, by testing the coupling strength under different waveguide spacing l, we can find that as the waveguide spacing l increases, the coupling strength c decays exponentially, as shown in Fig. 6:

$$c = 14.382e^{-0.345l}. \tag{B4}$$

For different waveguide propagation constants ($\Delta\beta = \beta_a - \beta_b \neq 0$):

$$\begin{aligned} \psi_a(z) &= [\cos(\kappa z) + i\frac{\Delta\beta}{2\kappa}\sin(\kappa z)]\psi_a(0) \\ &\quad + [i\frac{c}{\kappa}\sin(\kappa z)]\psi_b(0) \\ \psi_b(z) &= [\cos(\kappa z) - i\frac{\Delta\beta}{2\kappa}\sin(\kappa z)]\psi_b(0) \\ &\quad + [i\frac{c}{\kappa}\sin(\kappa z)]\psi_a(0), \end{aligned} \tag{B5}$$

where the global phase factor $e^{-i\beta z}e^{i\delta\beta/2}$ is ignored. And $\kappa = \sqrt{(\Delta\beta/2)^2 + c^2}$ is the effective coupling coefficient when $\Delta\beta \neq 0$. If waveguide a is excited alone, the photon probability distribution of waveguide b is

$$|\psi_b(z)|^2 = \frac{c^2}{\kappa^2}\sin^2(\kappa z) = \frac{c^2}{2\kappa^2} - \frac{c^2}{2\kappa^2}\cos(2\kappa z). \tag{B6}$$

The propagation constant is realized by modulating the refractive index of the waveguide, which can be tuned by scanning velocity or laser power. We accurately control the propagation constant by tuning the laser power. A laser power of 190 mW is set as the base power. Taking a change of 10 mW as an example, as shown in Fig. 7(a), we measure the intensity of the outgoing light spot under different coupling lengths. And then we obtain the parameters in Eq. (B6) ($x = c^2/2\kappa^2$, $y = 2\kappa$) by fitting the probability of the

outgoing light intensity distribution of waveguide b. Then the propagation constant difference can be calculated by

$$\Delta\beta = (1 - 2x)y^2. \tag{B7}$$

Further, by changing the laser power, we obtain that the propagation constant difference changes linearly with the laser power, as shown in Fig. 7(b):

$$\Delta\beta \sim 0.10 \times \Delta P. \tag{B8}$$

APPENDIX C: SIMULATION WITH DISORDER

Figure 8 shows a comparison of experiment and simulation, in which the experimental results (the red circle) are consistent with the simulation (the blue curve). The shaded region indicates one standard deviation away from the averaged localization level (the red circle) obtained from 100 simulations with disorder $c \pm 0.05$ mm^{-1} and $\beta \pm 0.05$ mm^{-1}, as shown in Figs. 8(a) and 8(b), respectively.

[1] R. Bistritzer and A. H. MacDonald, Moiré bands in twisted double-layer graphene, Proc. Natl Acad. Sci. USA **108**, 12233 (2011).

[2] D. Marchenko, D. V. Evtushinsky, E. Golias, A. Varykhalov, T. Seyller, and O. Rader, Extremely flat band in bilayer graphene, Sci. Adv. **4**, eaau0059 (2018).

[3] C. R. Woods *et al.*, Commensurate–incommensurate transition in graphene on hexagonal boron nitride, Nat. Phys. **10**, 451 (2014).

[4] Y. Cao, V. Fatemi, A. Demir, S. Fang, S. L. Tomarken, J. Y. Luo, J. D. Sanchez-Yamagishi, K. Watanabe, T. Taniguchi, E. Kaxiras, R. C. Ashoori, and P. Jarillo-Herrero, Correlated insulator behaviour at half-filling in magic-angle graphene superlattices, Nature **556**, 80 (2018).

[5] Y. Cao, V. Fatemi, S. Fang, K. Watanabe, T. Taniguchi, E. Kaxiras, and P. Jarillo-Herrero, Unconventional superconductivity in magic-angle graphene superlattices, Nature **556**, 43 (2018).

[6] Y. Saito, J. Ge, K. Watanabe, T. Taniguchi, and A. F. Young, Independent superconductors and correlated insulators in twisted bilayer graphene, Nat. Phys. **16**, 926 (2020).

[7] C. R. Dean, L. Wang, P. Maher, C. Forsythe, F. Ghahari, Y. Gao, J. Katoch, M. Ishigami, P. Moon, M. Koshino, T. Taniguchi, K. Watanabe, K. L. Shepard, J. Hone, and P. Kim, Hofstadter's butterfly and the fractal quantum Hall effect in moiré superlattices, Nature **497**, 598 (2013).

[8] P. San-Jose, J. González, and F. Guinea, Non-Abelian Gauge Potentials in Graphene Bilayers, Phys. Rev. Lett. **108**, 216802 (2012).

[9] L. A. Ponomarenko, R. V. Gorbachev, G. L. Yu, D. C. Elias, R. Jalil, A. A. Patel, A. Mishchenko, A. S. Mayorov, C. R. Woods, J. R. Wallbank, M. Mucha-Kruczynski, B. A. Piot, M. Potemski, I. V. Grigorieva, K. S. Novoselov, F. Guinea, V. I. Fal'ko, and A. K. Geim, Cloning of Dirac fermions in graphene superlattices, Nature **497**, 594 (2013).

[10] M. Serlin, C. L. Tschirhart, H. Polshyn, Y. Zhang, J. Zhu, K. Watanabe, T. Taniguchi, L. Balents, and A. F. Young, Intrinsic quantized anomalous Hall effect in a moiré heterostructure, Science **367**, 900 (2020).

[11] Y. Jiang, X. Lai, K. Watanabe, T. Taniguchi, K. Haule, J. Mao, and E. Y. Andrei, Charge order and broken rotational symmetry in magic-angle twisted bilayer graphene, Nature **573**, 91 (2019).

[12] X. Liu, Z. Hao, E. Khalaf, J. Y. Lee, Y. Ronen, H. Yoo, D. H. Najafabadi, K. Watanabe, T. Taniguchi, A. Vishwanath, and Philip Kim, Tunable spin-polarized correlated states in twisted double bilayer graphene, Nature **583**, 221 (2020).

[13] S. J. Ahn, P. Moon, T.-H. Kim, H.-W. Kim, H.-C. Shin, E. H. Kim, H. W. Cha, S.-J. Kahng, P. Kim, M. Koshino, Y.-W. Son, C.-W. Yang, and J. R. Ahn, Dirac electrons in a dodecagonal graphene quasicrystal, Science **361**, 782 (2018).

[14] K. Kim, A. DaSilva, S. Huang, B. Fallahazad, S. Larentis, T. Taniguchi, K. Watanabe, B. J. LeRoy, A. H. MacDonald, and E. Tutuc, Tunable moiré bands and strong correlations in small-twist-angle bilayer graphene, Proc. Natl. Acad. Sci. U.S.A. **114**, 3364 (2017).

[15] Y. Cao, J. Y. Luo, V. Fatemi, S. Fang, J. D. Sanchez-Yamagishi, K. Watanabe, T. Taniguchi, E. Kaxiras, and P. Jarillo-Herrero, Superlattice-Induced Insulating States and Valley-Protected Orbits in Twisted Bilayer Graphene, Phys. Rev. Lett. **117**, 116804 (2016).

[16] Y. Cao, D. Rodan-Legrain, J. M. Park, N. F. Q. Yuan, K. Watanabe, T. Taniguchi, R. M. Fernandes, L. Fu, and P. Jarillo-Herrero, Nematicity and competing orders in superconducting magic-angle graphene, Science **372**, 264 (2021).

[17] M. Yankowitz, S. Chen, H. Polshyn, Y. Zhang, K. Watanabe, T. Taniguchi, D. Graf, A. F. Young, and C. R. Dean, Tuning superconductivity in twisted bilayer graphene, Science **363**, 1059 (2019).

[18] B. L. Chittari, N. Leconte, S. Javvaji, and J. Jung, Pressure induced compression of flatbands in twisted bilayer graphene, Electron. Struct. **1**, 015001 (2019).

[19] S. Carr, S. Fang, P. Jarillo-Herrero, and E. Kaxiras, Pressure dependence of the magic twist angle in graphene superlattices, Phys. Rev. B **98**, 085144 (2018).

[20] R. Wang, P. Wang, K. L. Zhang, and Z. Song, Moiré pattern of a spin liquid and a Néel magnet in the Kitaev model, Phys. Rev. B **102**, 094207 (2020).

[21] R. Wang and Z. Song, Flat band and η-pairing states in one-dimensional Moiré Hubbard model, arXiv:2105.03615 (2021).

[22] O. Arroyo-Gascon, R. Fernandez-Perea, E. Suarez Morell, C. Cabrillo, and L. Chico, One-dimensional moiré superlattices and flat bands in collapsed chiral carbon nanotubes, Nano Lett. **20**, 7588 (2020).

[23] S. Zhao, P. Moon, Y. Miyauchi, K. Matsuda, M. Koshino, and R. Kitaura, Observation of Drastic Electronic-Structure Change in a One-Dimensional Moiré Superlattice, Phys. Rev. Lett. **124**, 106101 (2020).

[24] M. Koshino, P. Moon, and Y. -W. Son, Incommensurate double-walled carbon nanotubes as one-dimensional moiré crystals, Phys. Rev. B **91**, 035405 (2015).

[25] Q. Fu, P. Wang, C. Huang, Y. V. Kartashov, L. Torner, V. V. Konotop, and F. Ye, Optical soliton formation controlled by angle twisting in photonic moiré lattices, Nat. Photonics **14**, 663 (2020).

[26] P. Wang, Y. Zheng, X. Chen, C. Huang, Y. V. Kartashov, L. Torner, V. V. Konotop, and F. Ye, Localization and delocalization of light in photonic moiré lattices, Nature **577**, 42 (2020).
[27] R. A. Vicencio, C. Cantillano, L. Morales-Inostroza, B. Real, C. Mejía-Cortés, S. Weimann, A. Szameit, and M. I. Molina, Observation of Localized States in Lieb Photonic Lattices, Phys. Rev. Lett. **114**, 245503 (2015).
[28] S. Xia, A. Ramachandran, S. Xia, D. Li, X. Liu, L. Tang, Y. Hu, D. Song, J. Xu, D. Leykam, S. Flach, and Z. Chen, Unconventional Flatband Line States in Photonic Lieb Lattices, Phys. Rev. Lett. **121**, 263902 (2018).
[29] L. Lu, J. Joannopoulos, and M. Soljačić, Topological photonics, Nat. Photonics **8**, 821 (2014).
[30] T. Ozawa, H. M. Price, A. Amo, N. Goldman, M. Hafezi, L. Lu, M. Rechtsman, D. Schuster, J. Simon, O. Zilberberg, and I. Carusotto, Topological photonics, Rev. Mod. Phys. **91**, 015006 (2019).
[31] M. Hafezi, S. Mittal, J. Fan, A. Migdall, and J. M. Taylor, Imaging topological edge states in silicon photonics, Nat. Photonics **7**, 1001 (2013).
[32] X. Cheng, C. ouvaud, X. Ni, S. H. Mousavi, A. Z. Genack, and A. B. Khanikaev, Robust reconfigurable electromagnetic pathways within a photonic topological insulator, Nat. Mater. **15**, 542 (2016).
[33] Y. Plotnik, M. C. Rechtsman, D. Song, M. Heinrich, J. M. Zeuner, S. Nolte, Y. Lumer, N. Malkova, J. Xu, A. Szameit, Z. Chen, and M. Segev, Observation of unconventional edge states in 'photonic graphene', Nat. Mater. **13**, 57 (2014).
[34] Y. Lahini, A. Avidan, F. Pozzi, M. Sorel, R. Morandotti, D. N. Christodoulides, and Y. Silberberg, Anderson Localization and Nonlinearity in One-Dimensional Disordered Photonic Lattices, Phys. Rev. Lett. **100**, 013906 (2008).
[35] Y.-J. Chang, Y.-H. Lu, Y. Wang, X.-Y. Xu, W.-H. Zhou, W.-H. Cui, X.-W. Wang, J. Gao, L.-F. Qiao, and X.-M. Jin, Symmetry-Induced Error Filtering in a Photonic Lieb Lattice, Phys. Rev. Lett. **126**, 110501 (2021).
[36] Y.-H. Lu, Y. Wang, Y.-J. Chang, Z.-M. Li, W.-H. Cui, J. Gao, W.-H. Zhou, H. Zheng, and X.-M. Jin, Observing movement of Dirac cones from single-photon dynamics, Phys. Rev. B **103**, 064304 (2021).
[37] Y. Wang, J. Gao, X.-L. Pang, Z.-Q. Jiao, H. Tang, Y. Chen, L.-F. Qiao, Z.-W. Gao, J. -P. Dou, A.-L. Yang, and X.-M. Jin, Parity-Induced Thermalization Gap in Disordered Ring Lattices, Phys. Rev. Lett. **122**, 013903 (2019).
[38] K. M. Davis, K. Miura, N. Sugimoto, and K. Hirao, Writing waveguides in glass with a femtosecond laser, Opt. Lett. **21**, 1729 (1996).
[39] A. Szameit, F. Dreisow, T. Pertsch, S. Nolte, and Tünnermann, Control of directional evanescent coupling in fs laser written waveguides, Opt. Express **15**, 1579 (2007).
[40] H. Polshyn, M. Yankowitz, S. Chen, Y. Zhang, K. Watanabe, T. Taniguchi, C. R. Dean, and A. F. Young, Large linear-in-temperature resistivity in twisted bilayer graphene, Nat. Phys. **15**, 1011 (2019).
[41] Y. Zong, S. Xia, L. Tang, D. Song, Y. Hu, Y. Pei, J. Su, Y. Li, and Z. Chen, Observation of localized flat-band states in Kagome photonic lattices, Opt. Express **24**, 8877 (2016).
[42] S. Mukherjee, A. Spracklen, D. Choudhury, N. Goldman, P. Öhberg, E. Andersson, and R. R. Thomson, Observation of a Localized Flat-Band State in a Photonic Lieb Lattice, Phys. Rev. Lett. **114**, 245504 (2015).
[43] R. Osellame, G. Cerullo, and R. Ramponi, *Femtosecond Laser Micromachining: Photonic and Microfluidic Devices in Transparent Materials* (Springer, Berlin, 2012).
[44] Mor Verbin, Oded Zilberberg, Yaacov E. Kraus, Yoav Lahini, and Yaron Silberberg, Observation of Topological Phase Transitions in Photonic Quasicrystals, Phys. Rev. Lett. **110**, 076403 (2013).
[45] G. Corrielli, A. Crespi, G. D. Valle, S. Longhi, and Roberto Osellame, Fractional Bloch oscillations in photonic lattices, Nat. Commun. **4**, 1555 (2013).
[46] A. Rai, C. Lee, C. Noh, and D. G. Angelakis, Photonic lattice simulation of dissipation-induced correlations in bosonic systems, Sci. Rep. **5**, 8438 (2015).
[47] A. H. MacDonald, Bilayer graphene's wicked, twisted road, Physics **12**, 12 (2019).
[48] S. Wu, Z. Zhang, K. Watanabe, T. Taniguchi, and E. Y. Andrei, Chern insulators, van Hove singularities and topological flat bands in magic-angle twisted bilayer graphene, Nat. Mater. **20**, 488 (2021).
[49] R. A. Vicencio and C. Meja-Corts, Diffraction-free image transmission in kagome photonic lattices, J. Opt. **16**, 015706 (2014).
[50] S. Xia, Y. Hu, D. Song, Y. Zong, L. Tang, and Z. Chen, Demonstration of flat-band image transmission in optically induced Lieb photonic lattices, Opt. Lett. **41**, 1435 (2016).
[51] Y. Wang, X.-L. Pang, Y.-H. Lu, J. Gao, Y.-J. Chang, L.-F. Qiao, Z.-Q. Jiao, H. Tang, and X.-M. Jin, Topological protection of two-photon quantum correlation on a photonic chip, Optica **6**, 955 (2019).
[52] H. D. Raedt, A. Lagendijk, and P. d. Vries, Transverse Localization of Light, Phys. Rev. Lett. **62**, 47 (1989).
[53] T. Schwartz, G. Bartal, S. Fishman, and M. Segev, Transport and Anderson localization in disordered two-dimensional photonic lattices, Nature **446**, 52 (2007).
[54] M. Lebugle, M. Gräfe, R. Heilmann, A. Perez-Leija, S. Nolte, and A. Szameit, Experimental observation of N00N state Bloch oscillations, Nat. Commun. **6**, 8273 (2015).